In-situ-formed red phosphorus nanosheet on bulk red phosphorus for boosting charge separation in photocatalysis : The role of multiple interfacial effects

Fangyuan Chen [a],[1], Shoutian Sun [c],[1], Kelei Mu [a], Yi Li [d], Zhurui Shen [a],[b],[*], Sihui Zhan [a],[**]

[a] MOE Key Laboratory of Pollution Processes and Environmental Criteria, Tianjin Key Laboratory of Environmental Remediation and Pollution Control, College of Environmental Science and Engineering, Nankai University, Tianjin 300350, China
[b] School of Materials Science and Engineering, Nankai University, Tianjin 300350, China
[c] Department of Physics, Shanghai Normal University, Shanghai 200234, China
[d] Department of Chemistry, Tianjin University, Tianjin 300072, China

ARTICLE INFO

ABSTRACT

Red phosphorus (RP) has recently attracted much attention in photocatalysis for its low cost, environmental benign and optical properties. However, its photocatalytic activity is still restricted since the low-charge carrier mobility and the high water-solubility. Herein, RP-S-12 h (Combination of RP nanosheet (NS) and bulk RP structure) was prepared by hydrothermal method. Results showed that the multiple reactive active sites, the energy level matching, the emergence of intermediate state and the internal unequal potential for RP-S-12 h ensured higher charge density and efficient carrier transport, improving the photocatalytic activity and stability, emphasizing the role of multiple interfacial effects. The optimum hydrogen evolution rate was 0.33 mmol g^{-1} h^{-1}, and the quantum efficiency at 420 nm is 0.45%. In addition, RP-S-12 h could completely degrade 50 ppm MO in 12 min. This study provides a novel insight into the interface design of metal-free photocatalyst for environmental remediation.

1. Introduction

Solar-to-hydrogen (H_2) conversion has been deemed as the one of the most charming strategies to solve the environmental issues and the global energy crisis [1–3]. Accordingly, photocatalytic technology has also been widely used to degrade organic pollutants, reduce heavy metal ions, and realize self-cleaning [4–6]. For the conventional biophysical and chemical treatments (adsorption, microorganisms, flocculation, etc.), recalcitrant organic contaminant (Such as organic azo dyes, methyl orange) cannot be completely degraded. And their breakdown products tend to pose a threat to human health due to its carcinogenicity and teratogenicity [7–9]. Then, advanced oxidation processes (such as Fenton, Fenton-like and photocatalytic oxidation processes) are often employed to treat recalcitrant organic contaminant in wastewater as a promising solution. However, Fenton and Fenton-like oxidation

processes are often limited by the concentration or the kind of simple peroxides like H_2O_2, PA, HSO_5(peroxymonosulfate; PMS), and $S_2O_8^{2-}$ (peroxydisulfate; PDS) [10,11]. Therefore, the photocatalytic method has received extensive attention due to its cleanness, high efficiency, mild reaction conditions, and thorough degradation. Metal-based semiconductor photocatalyst is an efficient and stable photocatalyst, but it is easy to cause secondary pollution and suffer from high-costs. Among many semiconductor photocatalysts, non-metallic photocatalysts have attracted extensive attention because of their earth abundance, low toxicity and environmental friendliness. Non-metallic photocatalysts such as g-C_3N_4 [12], black phosphorus (BP) [13], RP [14] and boron [15] have good application prospects on account of their simple structure. However, photocatalytic activity has been limited since the narrow solar light response range and low charge separation/transfer efficiency for a long time [1,15]. Hence, it is of great

---

practical significance to further develop novel non-metallic high--performance photocatalysts for water splitting and degradation of organic pollutants.

RP has attracted much attention because of its rich natural resources, low-cost, environmental protection and excellent chemical stability at room temperature compared with BP and white phosphorus (WP) [16]. Although red phosphorus has a wide light absorption range (~700 nm), its conductivity is poor and the photogenerated carrier separation is low [17–19]. In terms of these problems, crystalline RP was prepared in our previous work [20,21]. Other studies prepared nano-RP and added co-catalyst (Pt) or semiconductor photocatalysts to facilitate the mobility of photogenerated electrons, effectively promoting the photocatalytic activity [22,23]. However, the nano RP often has poor stability in water environment and difficult to separate with water, and the introduction of metal material is likely to arouse secondary pollution, causing the high cost. Photo-generated charge separation rate for RP needs to be further improved. Thus, this inspired us to think that using the bulk red phosphorus to improve the stability of nano red phosphorus, promoting the stability of the material while retaining the role of nano RP in photocatalysis. Moreover, energy level matching can be formed between the bulk and nanosheet (NS) of RP, providing the benefits for the enhancement of charge separation rate in multiple interface factors.

Herein, we prepared ultra-thin red phosphorous nanosheets/bulk red phosphorous composites (RP-S-12 h) by a simple hydrothermal method, aiming to explore the role of multiple interfacial effects in boosting photocatalytic hydrogen production and the degradation activity. The hydrogen evolution rate of composite (0.33 mmol $g^{-1} h^{-1}$) was 5.8 times and 2.0 times higher than RP bulk and NS under visible light, respectively. The composite could completely degrade methyl orange (MO) in 12 min, while the bulk RP degraded by 54.7% in 12 min. Moreover, hydrogen production of composite could still reach the initial 91.4% after three cycle experiments. Combined with the theoretical calculation and experimental characterization of photocatalysts, results showed that: 1) The band matching between bulk RP and RP NS effectively facilitated the photocatalytic activity. 2) The internal different potential in RP-S-12 h could provide driving force for the transfer of photogenerated electrons from bulk RP to RP NS. 3) The capping of the surface oxygen-containing functional groups (P-O-P, P=O, P-OH) in the ultrathin RP NS promoted the appearance of intermediate state, supplying a new electron transfer path and further boosting the separation rate of photogenerated charges.

2. Experimental sections

2.1. Preparation of RP-S

Commercial RP (3 g; Supplied from Saen Chemical Technology Co., Ltd.) was purified with hydrothermal method for removing surface oxides [24], which is identified as RP. Then, for the secondary hydrothermal: RP (1 g) was added into the 60 ml deionized water to obtain uniformly dispersed solution via 5 min stirring, and hydrothermally treated at 200 °C for x hours in a 100 ml autoclave for obtaining RP-S-x h (x = 4, 8, 12, 16).

0.5 g RP-S-12 h was added into 500 ml deionized water for 8 h ultrasound to acquire RP nanosheet. Then, the upper supernatant was obtained via centrifugation process (3000 r/min for 10 min). Finally, the supernatant was precipitated by high-speed centrifugation (12000 r/min for 5 min) for further characterization, which deemed as RP NS. In addition, RP NS prepared by stirring method was used to exclude the damage impact caused by ultrasound (Detailed see Section 1 in Supporting information: Figs. S1-S3).

To further determine the specific content of RP NS on the RP-S-x h samples, 0.5 g RP-S-x h were added into 500 ml water and stirred for 8 h to obtain RP NS in the supernatant. Among them, RP-S-x h (x = 4, 8, 12 and 16) had 2.3 wt%, 3.56 wt%, 5.40 wt% and 6.83 wt% NS,

respectively. For comparation, the same operation was employed for bulk RP (0.59 wt%).

2.2. Characterization

The crystal structure of samples was determined with X-ray diffraction patterns (XRD) on Rigaku D/Max 2200PC X-ray diffractometer with Cu Kα radiation. The UV–vis spectrophotometer (Shimadzu UV-360003040425) was employed to acquire the spectra of the as-prepared samples. Raman spectrum were performed on a Horiba Raman microscope with excitation laser beam wavelength of 532 nm. Steady-state photoluminescence (PL) spectra were performed using an Edinburgh Instruments FLS920P equipped with a Xe lamp-920 at room temperature under the excitation of 316 nm. X-ray photoelectron spectroscopy were measured in a Thermo scientific Xi$^+$ electron spectrometer using Al Kα X-ray source under ultrahigh vacuum (5×10^{-8} Pa). The binding energy was calibrated with polluted carbon C_{1s} (284.4 eV as correction value). The morphology of the composites was collected on scanning electron microscopy (SEM, Hitachi SU8010 at an accelerating voltage of 3 kV (Japan)) and High-resolution transmission electron microscopy (HRTEM) analysis (JEOL JEM-2100 F at an accelerating voltage of 200 kV (Japan)). The thickness of photocatalysts was recorded on the atomic force microscopy (AFM) measurement using Bruker's Dimension Icon Atomic Force Microscope System. Kelvin probe force microscopy (KPFM) map was conducted on the contact potential difference (CPD), estimating the work function difference between tip and surface. The CPD between probe tip and sample is defined as [25]:

$$CPD = \left(\frac{\varphi_{tip} - \varphi_{sample}}{e} \right) \tag{1}$$

Note: ϕ_{tip} and ϕ_{sample} are the work function for the tip and the sample, respectively. e is the elementary charge.

The photoelectrochemical analysis was collected on CHI760E electrochemical workstation with a Pt plate (counter electrode) and saturated calomel electrode (reference electrode). The carrier density N_d can be determined via Mott-Schottky plots using the following equation [26]:

$$N_d = \left(\frac{2}{e\varepsilon\varepsilon_0} \right) \left[\frac{d(E_S)}{d\left(\frac{1}{C^2}\right)} \right] \tag{2}$$

Note: C is the space charge capacitance in the semiconductor, N_d is the electron carrier density, e is the elemental charge value, ε is the relative permittivity of the semiconductor, E_s is the applied potential.

2.3. Photocatalytic H_2 production activity

The 100 ml solution of 0.25 M Na_2S (Shanghai Meryer Chemical Technology Co., Ltd) and 0.35 M Na_2SO_3 (Shanghai Aladdin Bio-Chem Technology Co., Ltd.) was used as sacrificial electron donor model with 30 mg samples (supported by Beijing CEAULIGHT. Inc, product model: CEL-PAEM-D8. Detector: TCD and carrier gas: Argon). 300 W Xe lamp with a UV-cut 420 nm filter as light source and the area of the surface irradiated in quartz cylindrical reactor was about 31 cm^2. The suspension was illuminated under continuous magnetic stirring after thoroughly degassed by evacuation at 10 °C. Next, automatic injection of the reaction system every 30 min

The quantum efficiency (QE) at the wavelength of 420 nm, 475 nm and 520 nm were measured under the identical reaction condition by placing various band-pass filters in front of the light source. The CEL-NP2000 spectroradiometer was used to measure the intensity of the incident light. The QE was calculated according to the following equation [26].

$$QE(\%) = \frac{number\ of\ evolved\ H_2\ molecules \times 2}{number\ of\ incident\ photons} \times 100 = \frac{mmol \times N_A \times 10^{-3} \times 2}{\frac{I \times A \times t}{E_g \times J}} \times 100\% \tag{3}$$

Note: $N_A = 6.02 \times 10^{23}$. I is the light intensity. A (31 cm^2) is the light-receiving area. t is time, $J = 1.6 \times 10^{-19}$. $E_g = \frac{1240}{\lambda}$.

2.4. Photocatalytic degradation of MO

300 W Xenon arc lamp with a UV cutoff (CEL-HXF300, $\lambda > 420$ nm) was used as the light source. In a typical visible light test, 30 mg photocatalyst was dispersed in MO solution (50 ml 50 ppm) with stirring for 30 min for reaching adsorption-desorption equilibrium. The 3 ml suspension was sampled and filtered through a 0.22 μm nylon membrane every 30 min. Further measurements were evaluated using UV-Vis spectrophotometers at 463 nm. The surface functional groups on the as-prepared samples and samples after adsorption of MO were identified by Fourier transform infrared spectroscopy (FT-IR, Bruker Optics Invenio-S). Furthermore, the ability of the samples to produce superoxide anion was evaluated via nitroblue tetrazole (NBT) test [27]. Different types of trapping agents were used to detect the active substances that cause the degradation of pollutants. The superoxide radical ($\bullet O_2^-$) and hydroxyl radicals ($\bullet OH$) were also detected via electron paramagnetic resonance (EPR) spectroscopic tests. In detail, the as-prepared sample was added to the methanol solution (1 mg/l), followed by the 5, 5-dimethyl-pyrroline-N-oxide (DMPO) solution (50 mM). Pipette the solution into the Bruker EMX PLUS instrument with a capillary. Then, acquire the EPR signal of $\bullet O_2^-$ at regular intervals on 300 W Xe lamp with a UV-cut 420 nm filter. Furthermore, the EPR signal of $\bullet OH$ was also collected using this method except that the methanol solution was replaced by deionized water. Ion chromatography (Thermo Fisher: ICS5000) with a AS16 column was employed to detected the concentration of phosphorus by-products leaching from the possible dissolution of the as-prepared samples using KOH as the eluent. The concentration of phosphite (3$^+$), phosphate (5$^+$) and pyrophosphate (5$^+$) ions were detected by using 30 mg of bulk RP and RP-S-12 h with pure water under the visible light after 12 h. What's more, since RP NS was obtained via ultrasonic method of RP-S-12 h, the leaching ions concentration of RP NS was the data measured by ultrasonic residual liquid minus the ion concentration of bulk RP under the visible light after 12 h.

2.5. Theoretical calculation

First-principle calculations were performed with density functional theory (DFT) as implemented in the Vienna *ab*-initio Simulation Package (VASP) package [28]. The interactions between ions and valence electrons were described by the augmented wave (PAW) method [28,29], with the generalized gradient approximation (GGA) type of Perdew-Burke-Ernzerhof (PBE) functional for the electronic exchange and correlation interactions [30]. A kinetic energy cutoff of 450 eV was selected for the plane wave basis set. A sufficiently large vacuum layer of 20 Å were used to avoid the artificial image interactions between slabs along *z*-direction. The atomic force and energy convergence criteria thresholds were set as 2×10^{-2} eV and 1×10^{-5} eV/Å, respectively. The k-point mesh of $3 \times 3 \times 1$ was employed for the geometric optimization and density of states (DOS) calculations. The Van der Waals (VdW) interactions between layers were also considered with Grimme type at DFT-D3 level [31] for all of the simulations.

3. Results and discussion

3.1. Characterization of catalysts

Herein, the RP-S composite photocatalyst was synthesized via a simple secondary hydrothermal method using the commercially RP as the starting material in Fig. 1a. It clearly showed that the colors of the samples became lighter and more orange with the increase of secondary hydrothermal time. The SEM and TEM images of RP material exhibited a large bulk with some finely stacked layered structure (Figs. 1b, 1c and Fig. S4). However, significant ultra-thin flakes were formed on the RP surface after 12 h for hydrothermal method (Fig. S5). Accordingly, the same phenomenon was also shown in TEM image (Fig. 1d). In Fig. 1e, the structure of ultra-thin NS was amorphous. RP NS was used as a comparative sample via ultrasonic method (Fig. S6). The HAADF-STEM and the corresponding energy dispersive spectroscopy (EDS) analysis displayed that the O element of RP-S-12 h was increased compared with RP, further illustrating the generation of oxidative RP NS on bulk RP (Fig. 1f, g, j, k and Figs. S6-S9). The AFM analysis confirmed that the thickness of the small surface layer was ~1.66 nm, which was thinner than the original bulk RP (~3.63 nm) (Fig. 1h, i, l, m and Fig. S10). These results might indicate that the RP on the surface could be stripped from bulk to the ultra-thin NS via the secondary hydrothermal treatment. Moreover, the generation of the RP NS on bulk RP have been further explored from the point of crystal growth. The water could promote the formation of RP NS and the hydrothermal process could accelerate its formation (Detailed see Section 2 in Supporting information: Figs. S11 and S12).

The XRD patters showed that the crystal structure and phase composition of as-prepared samples were amorphous (Fig. 2a) [16], which was consistent with HRTEM images. In Fig. 2b, the three characteristic Raman peaks of amorphous RP at 345.7, 385.2–400.8 and 451.3 cm^{-1} could be indexed to the fundamental mode (B1), symmetric stretch modes (A1) and degenerate mode (E1) of RP, respectively [32]. However, the intensity of B1, A1 and E peak decreased significantly after the secondary hydrothermal and there was a significant (5 cm^{-1}), clarifying the increase in disorder and polarization for RP-S-12 h composite. The Raman spectroscopy of RP-S-12 h after ultrasound also exposed the same phenomenon, which was identical with our previous report [33], ascribing to the phonon confinement effect of the as-exfoliated NS and inferring their ultrathin thickness [34].

To further explore the chemical environment around the phosphorus element for RP-S, the XPS analysis was employed (C$_{1s}$ standard peak was calibrated with 284.4 eV). The presence of C$_{1s}$, O$_{1s}$ and P$_{2p}$ signals in the survey spectra of RP, RP-S-12 h and RP NS exhibited the high purity of phosphorus (Fig. 2**c** and Fig. S13). RP-S-12 h (131.1 and 130.1 eV) and RP NS (131.0 and 130.0 eV) had a slight red shift compared the bare RP (130.9 and 129.9 eV) for P$_{2p}$ spectra (Fig. 2d and Fig. S13), suggesting that the electron cloud density around the surface P atoms decreased for RP-S-12 h [35,36]. Interestingly, RP NS (15.2%) exhibited the maximum degree of oxidation compared to RP (10.2%) and RP-S-12 h (11.6%) (The ratio of the peak area of red phosphorus oxide to the total area of P 2p (The inner of Fig. 2d)) [37]. This result indicated that the surface of RP-S-12 h was partially oxidized and the increase of O content might promote the accumulation of electrons on the surface. Correspondingly, the 534.0, 532.7 and 532.1 eV was attributed to the P=O, P-O-P, P-OH in the O$_{1s}$ XPS spectra for the RP-S-12 h composites (Fig. 2e) [16,38]. The analysis of FT-IR spectra of the samples also proved these results (Fig. 2f). The peaks centered at about 3440 cm^{-1} and 1643 cm^{-1} could
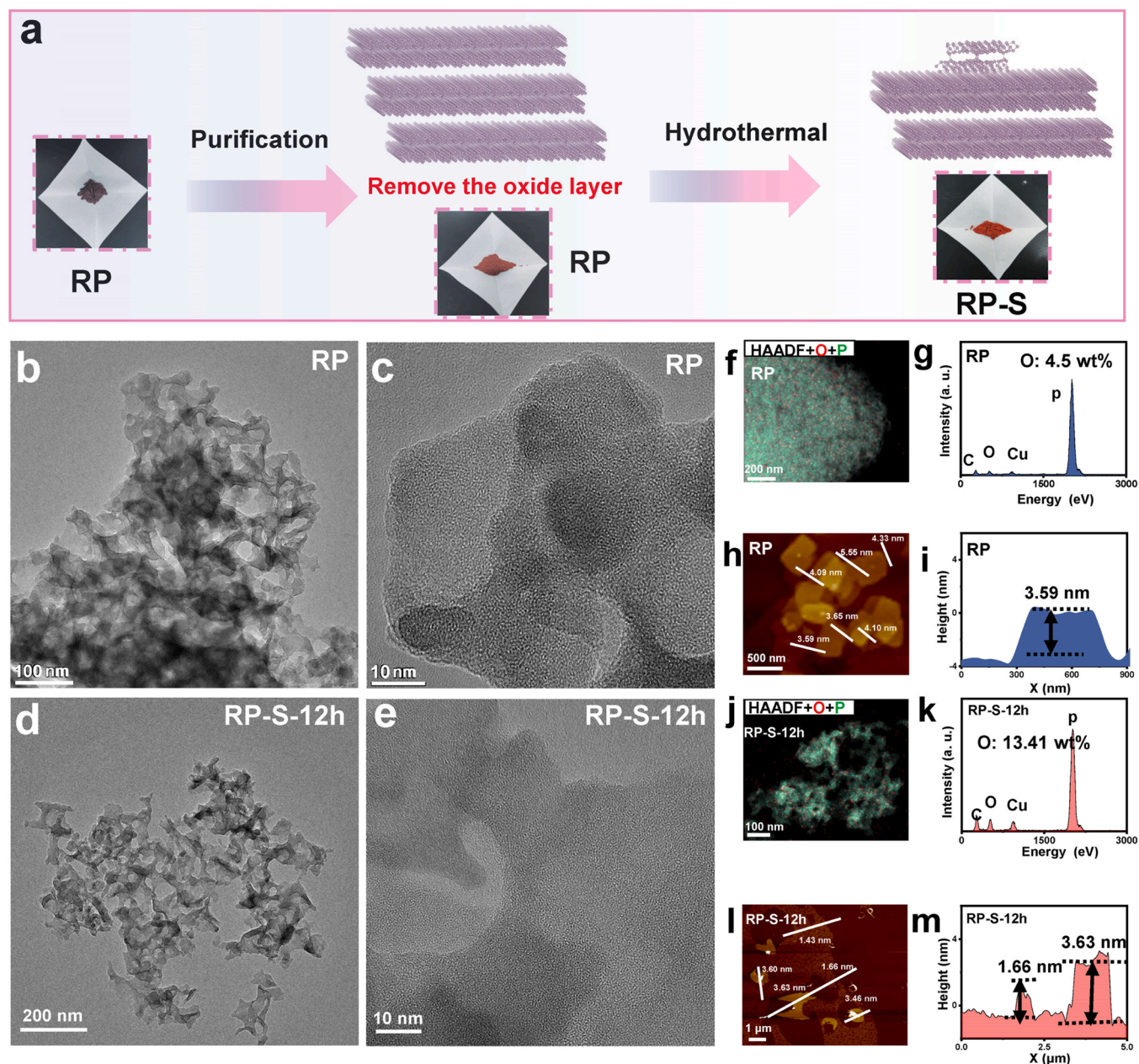
Fig. 1. (a) Schematic diagram of the synthesis process of h. (b) TEM and (c) HRTEM images of RP. (d) TEM and (e) HRTEM images of RP-S-12 h. (f) HAADF STEM + P element + O element mapping image and the (g) EDS analysis of RP. (h) AFM images and (i) the corresponding height plots of RP. (j) HAADF STEM + P element + O element mapping image and the (k) EDS analysis of RP-S-12 h. (l) AFM images and (m) the corresponding height plots of RP-S-12 h.

be assigned to the -OH vibration and bending mode of the adsorbed water on the surface of samples, respectively. The peaks at 1158 cm^{-1} and 1002 cm^{-1} in the spectrum of samples represented the P=O and P-O-P stretching mod, respectively [39,40]. Obviously, the oxidation peak of RP NS and RP-S-12 h was stronger than that of RP, being consistent with the results of XPS analysis and EDS analysis. The contact angle test results illustrated that the increase of increase of O content (P=O, P-O-P and P-OH) enhanced the wettability for RP-S-12 h and RP NS (Fig. 2g-i) [41].

3.2. Efficient photocatalytic H$_2$ production and MO degradation over RP-S-12 h

The photocatalytic degradation of methyl orange and hydrogen evolution was applied to verify the relationship of structure-activity. The sustained hydrogen production plots and hydrogen evolution rate diagrams of different materials were shown in Fig. 3a and b under visible light, respectively. Compared with other different hydrothermal materials, the RP-S-12 h displayed the best photocatalytic hydrogen production activity (1.00 mmol g^{-1} after 3 h), which was 5.8 and 2.0 times higher than that of RP and RP NS, further confirming that the presence of a thin layer of RP on the surface after the secondary hydrothermal process could significantly elevate the photocatalytic hydrogen production activity. It showed that 5.40 wt% RP NS in the bulk RP was optimal content in photocatalytic activity. RP-S-12 h displayed the highest quantum efficiency (0.45%) at 420 nm than RP and RP NS (Fig. S14). Moreover, hydrogen production of photocatalysis could still reach 91.4% of the initial hydrogen production after three cycle experiments (Fig. 3c). The XRD and Raman results had not changed significantly after photocatalytic hydrogen evolution, suggesting the
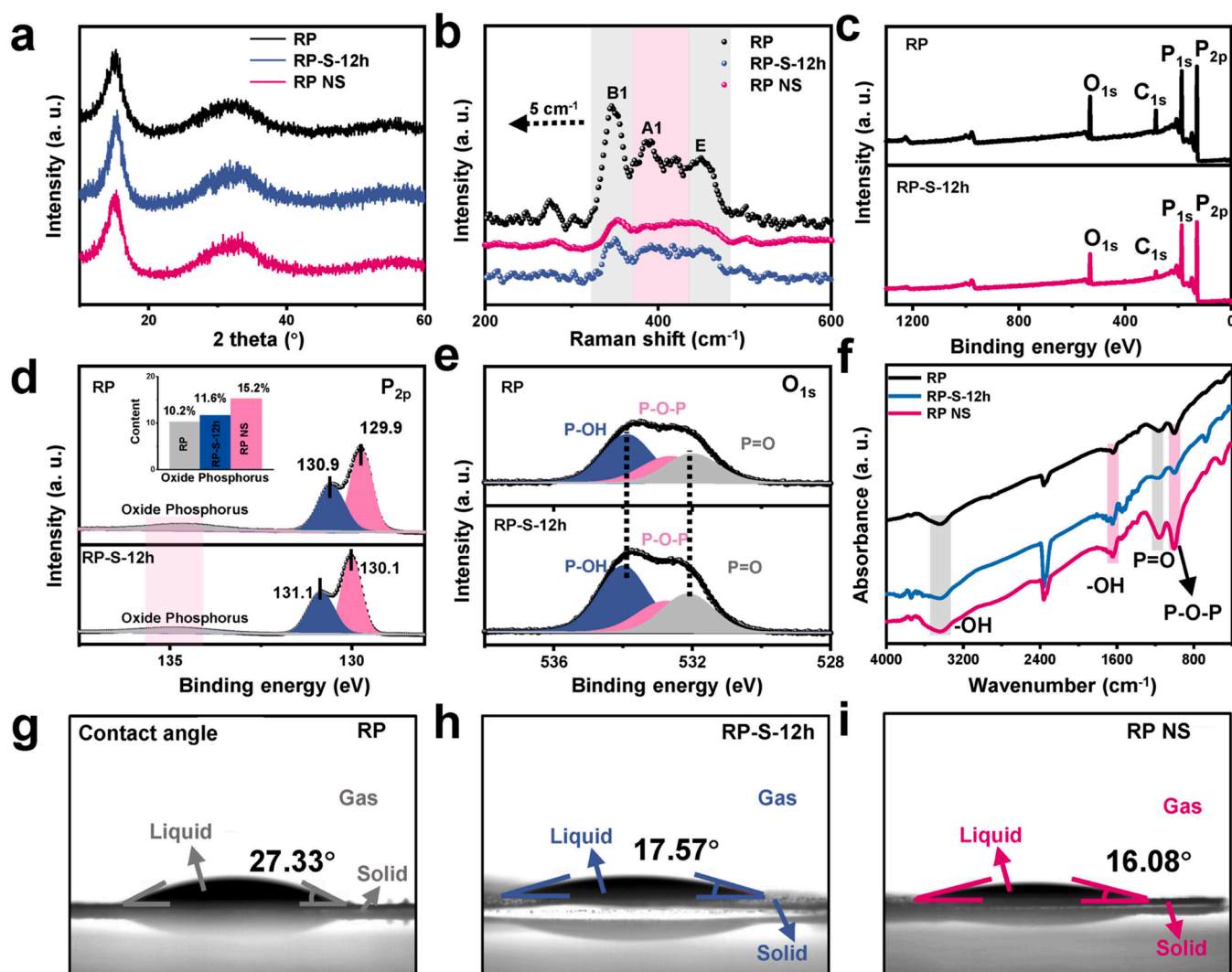
Fig. 2. (a) The XRD patterns and (b) the Raman spectra of the as-prepared samples. The survey spectra of and (c) RP and RP-S-12 h. XPS spectra of (d) P_{2p} and (e) O_{1s} for the RP and RP-S-12 h. (f) The FT-IR spectra of RP, RP-S-12 h and RP NS. Contact angle measurement of a water droplet on (g) RP (h) RP-S-12 h and (i) RP NS after 2 seconds.

good stability for RP-S-12 h (Fig. S15 and Fig. S16).

Then, the similar photocatalytic degradation trends of MO could also be observed in Fig. 3d. RP-S-12 h could completely degrade 50 ppm MO in 12 min, while the degradation rate of MO was only 54.7% for RP. The degradation rate of RP-S-12 h was 8.60 and 2.39 times that of RP and RP NS (Fig. 3e). Moreover, to understand the difference in adsorption capacity of samples, the Brunauer-Emmett-Teller (BET) specific surface area and FT-IR analysis were adopted. The BET specific surface area of RP NS and RP-S-12 h were calculated to 37.7 m^2 g^{-1} and 10.4 m^2 g^{-1} with 14.5-fold and 4.0-fold increase relative to pristine RP (2.6 m^2 g^{-1}) (Fig. S17), demonstrating the improvement of adsorption site for RP NS and RP-S-12 h, which indicated that the RP NS was more susceptible to oxidation compare with pristine RP when facing air or oxidant. Hence, the increase oxygen on the surface of RP-S-12 h and RP NS compared with bulk RP, which could also be proven by the analysis of XPS and EDS plots. In Fig. S18, the peak at 1158 cm^{-1} and 1002 cm^{-1} shifted to the peak at 1180 cm^{-1} and 1008 cm^{-1} after adsorption of MO, which could be assigned to two reasons: 1) The asymmetric stretching vibration in the -SO_3Na group, indicating that MO is adsorbed on the surface of the material. 2) The shift also suggested that the enhanced the electrostatic interaction between cationic MO and as-prepared samples [42]. In addition, the peak at 1643 cm^{-1} for -OH shift to 1653 cm^{-1} for the samples after adsorption, suggesting that MO was successfully attached to these photocatalysts through hydrogen bonding [43]. In addition, compared with the bulk RP and RP NS, the strength of the peak at 1653 cm^{-1} for RP-S-12 h displayed the strongest -OH stretching mode vibration after adsorption of MO, suggesting that the strong adsorption capacity of RP-S-12 h.

Typically, Fig. 3f displayed the time-dependent UV-Vis absorption measurement of MO degradation. It was observed that the dye was completed decolorized in about 12 min and a new peak appeared at ~248 nm, demonstrating that cleavage of the azo bond (Chromophoric group: -N=N-) and the formation of aromatic products (-NH_2) over reaction time [44]. Furthermore, the intensity of this absorption peak at ~248 nm exhibited a trend of rising first and then falling at 24 min, supporting the formation of small molecules and it also could be degraded. To further explore the detailed form of this small molecule, the reaction solution was analyzed via HPLC-MS, which proved that the small molecules were produced and the pollutants could be mineralized into CO_2 and water (Fig. S19). In addition, MO could still reach 100% after three cycles for RP-S-12 h in 12 min, while the degradation rate of RP NS was 89.4% of the original RP NS after 3 cycles (Fig. 3g), supporting that the RP-S-12 h has good stability. What's more, red phosphorus as a reductant would conduct self-transformation and produce various phosphorus by-products (phosphite (3^+), phosphate (5^+) and pyrophosphate (5^+)) [45–47]. The concentrations of phosphite,
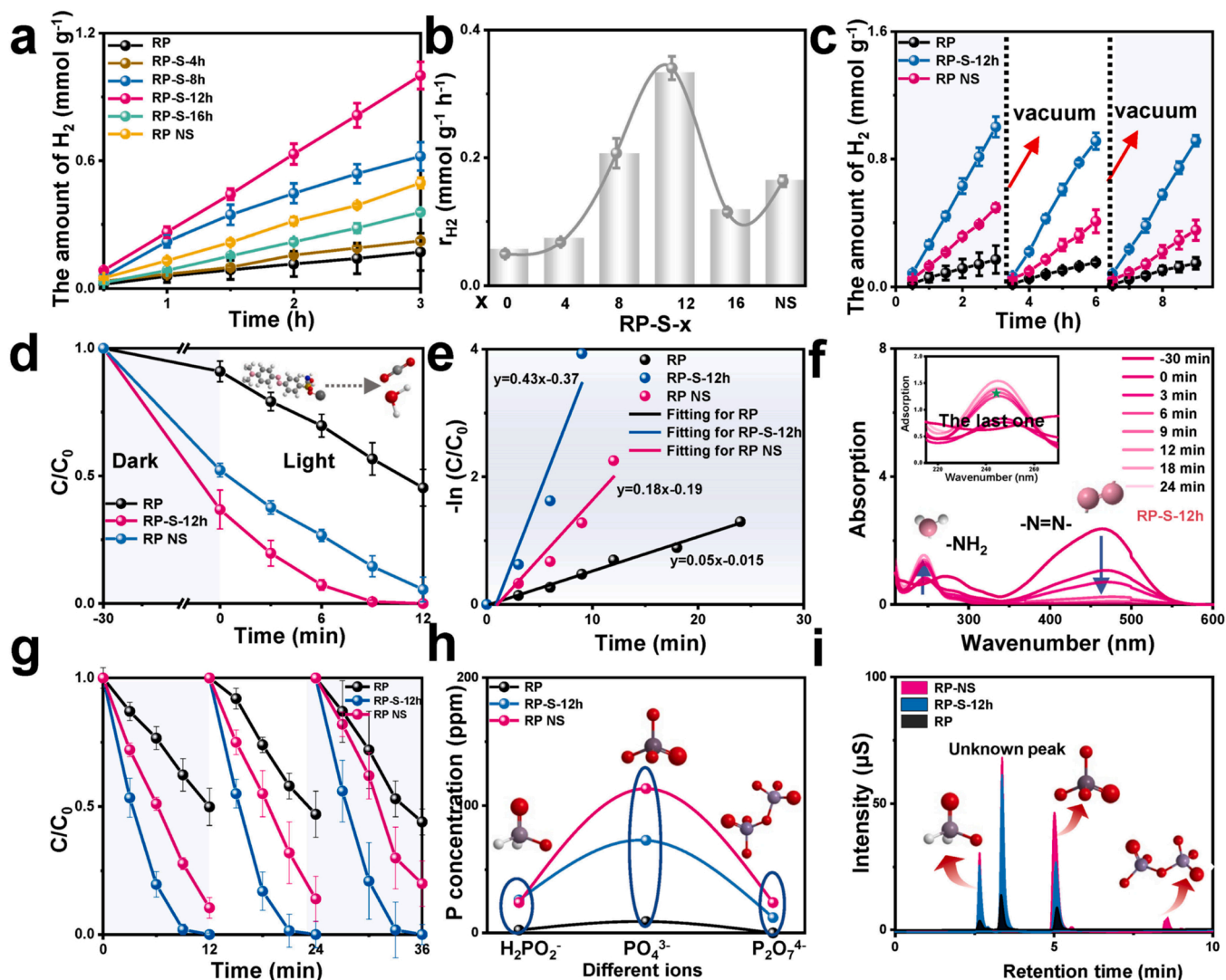
Fig. 3. (a) The photocatalytic H₂ evolution of as-prepared samples in Na₂S/Na₂SO₃ solution. (b) The H₂ evolution rate of as-prepared samples. (c) The cyclic experiment of different samples for photocatalytic hydrogen evolution. (d) Visible-light-driven photocatalytic degradation and (e) the degradation rate for MO over different samples. (f) Absorption spectra variations of MO solution system over the RP-S-12 h. (g) The cyclic experiment of different samples for MO degradation. (h) The concentration of phosphite (3^+), phosphate (5^+) and pyrophosphate (5^+) ions and (i) the corresponding ion chromatograms by using 30 mg of the as-prepared samples with pure water under the visible light after 12 h.
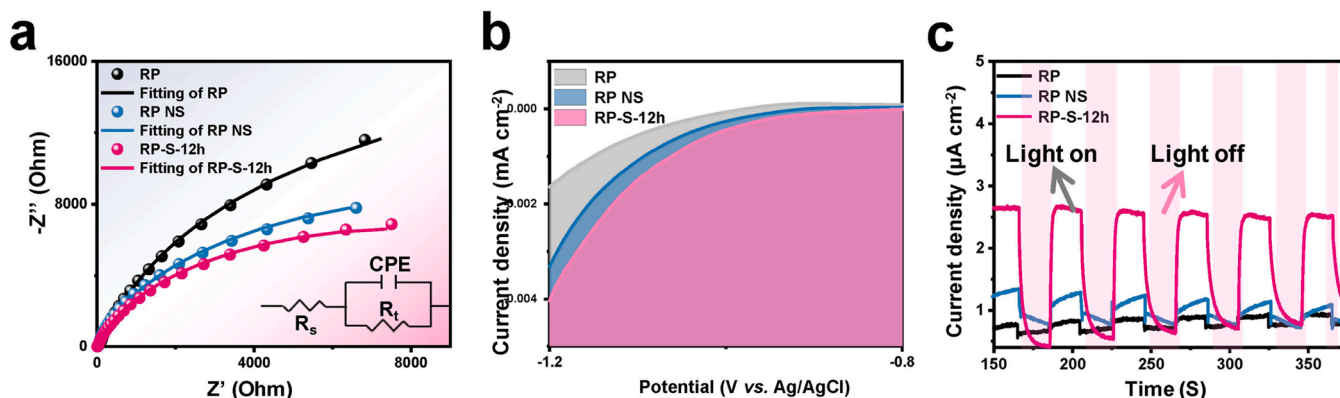

Fig. 4. (a) The EIS and (b) the LSV spectra of the various samples. (c) The transient photocurrent responses of RP, RP-S-12 h and RP NS.

phosphate and pyrophosphate were measured with deionized water by ion chromatography. In Fig. 3h and i, the phosphate concentration for RP NS (113.24 ppm) is 1.55 and 12.5 times that of bulk RP and RP-S-12 h, which might be ascribed to the high specific surface area and the oxygen content for RP NS, suggesting that RP-S-12 h maintained the performance of the bulk RP that was not easy to self-transformation. Combined with the photocatalytic measurements, the bulk RP could enhance the stability of RP NS.

3.3. Mechanism discussion

Moreover, the electrochemical impedance spectroscope (EIS), linear sweep voltammetry (LSV) spectra and photocurrent curve was explored to obtain a deep insight into the charge transfer and separation processes. Thus, in Fig. 4a, EIS spectra were analyzed and the equivalent circuit of the devices for RP, RP-S-12 h, RP NS photocatalysts. R_s (the electrolyte solution resistance) and R_t (the interfacial charge-transfer resistance) represented the series resistance of the system. RP-S-12 h had the smallest semicircle radius and the smallest Rt (16.76 kΩ) value

compared to bulk RP (40.30 kΩ) and RP NS (18.45 kΩ), demonstrating that the RP-S-12 h had more effective electronic transfer of interfacial charge-transfer resistance [48]. The highest current density of RP-S-12 h exhibited over those of RP bulk and RP NS in the LSV plots of the current density versus the potential (J-V) (Fig. 4b), demonstrating the best property for H_2 generation. The correlation of the optical characterization was also revealed the photocurrent [21]. Subsequently, the photocurrent of RP-S-12S was 11.2 times and 5.6 times of bulk RP and RP NS (Fig. 4c). In addition, the KPFM measurement was used to directly observe the direction of electron transfer based on the different potential combined with AFM images. As shown in Fig. 5a, the ultra-thin RP NS (~1.6 nm: ~ −25.22 mV) has a lower potential than the bulk RP (~ 3.8 nm: ~ −11.28 mV) based on the silicon wafer (0 mV), indicating that the photo-generated electrons transferred from the bulk RP to the ultra-thin nanosheets RP [25,49]. Correspondingly, the stacked structure appeared in the Fig. 5b for the bulk RP, and its relative potential for RP (~ −10.06 mV) also showed a similar potential to that of bulk RP (~ −11.28 mV). Nevertheless, RP displayed no obvious difference in the plane except for comparing with silicon wafer. These phenomena could
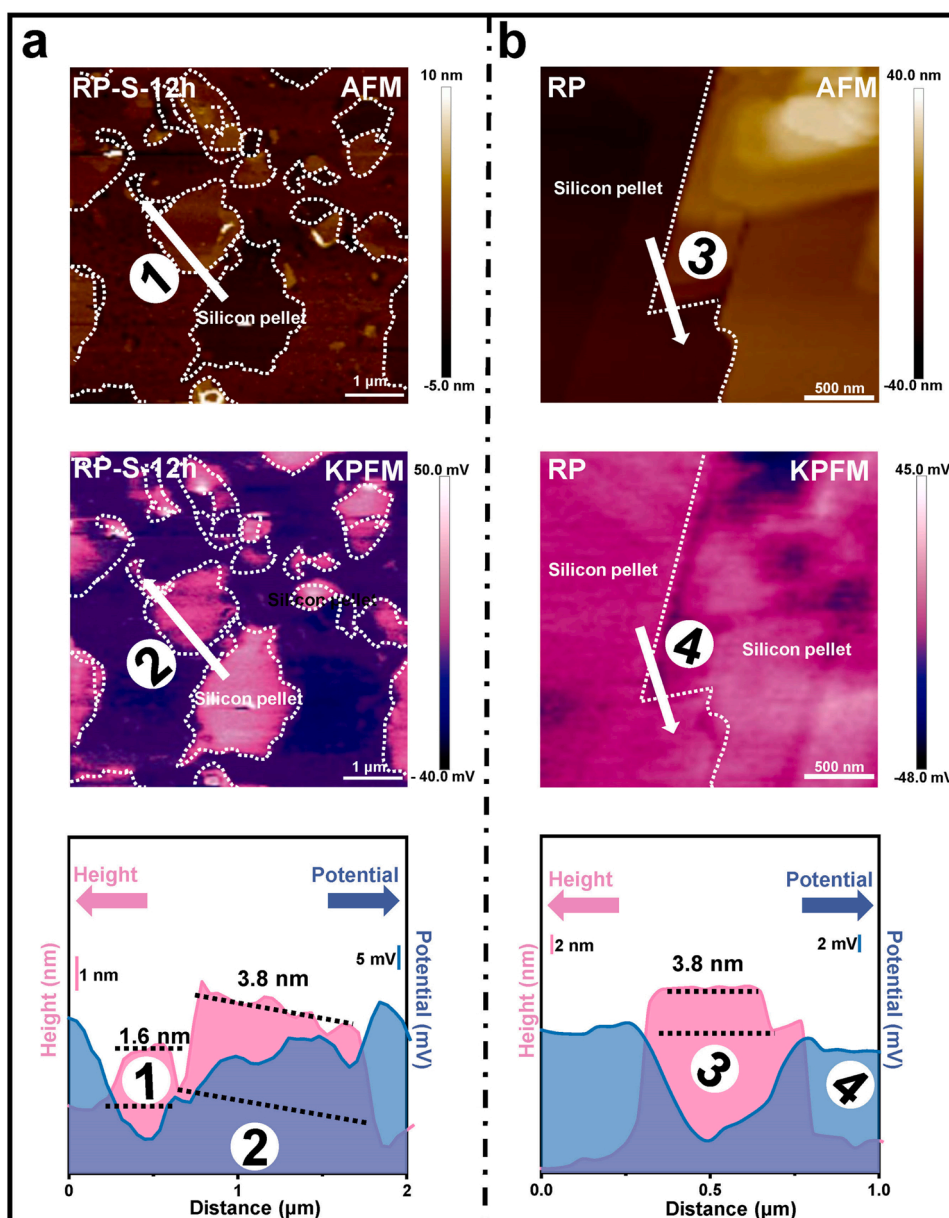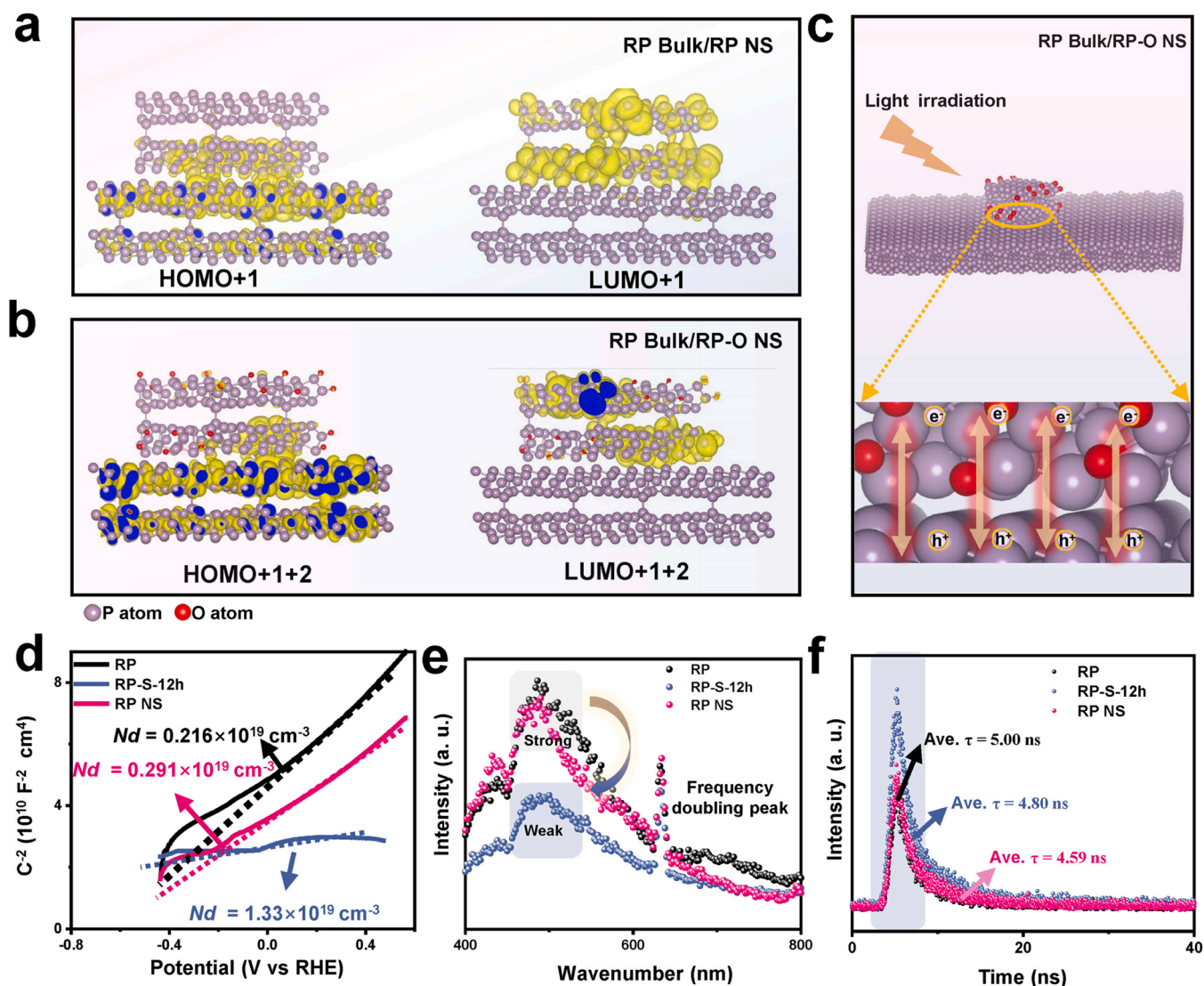

Fig. 5. AFM images, KPFM images and the corresponding height/potential profiles over (a) RP-S-12 h and (b) bulk RP.

Fig. 6. Spatial distributions of HOMO and LUMO of the (a) RP NS/bulk RP and (b) RP-O NS/bulk RP. (c) Schematic diagram of charge transfer for RP-O NS/bulk RP under visible light irradiation. (d) Mott-Schottky relationship, (e) the photoluminescence (PL) emission spectra and (f) the time-resolved photoluminescence spectroscopes of RP, RP-S-12 h and RP NS.

also serve as the direct evidence for the steered electron transfer from bulk RP to the RP NS.

Therefore, to gain insight into the high charge separation efficiency, the highest occupied molecular orbital (HOMO) and lowest unoccupied molecular orbital (LUMO) of the RP NS on the bulk RP were calculated to investigate the charge distribution (Fig. 6a-c, Fig. S20 and S21). Obviously, the HOMO and LUMO locations were highly scattered on the bulk RP and RP NS (Fig. 6a) [50], which was consistent with previous activity test and photoelectrochemical results. Moreover, since phosphorus reacts with oxygen when facing air or oxidant, one of the main problems with photocatalysts made from pure phosphorus was stability, which have been observed in many studies on the black P and red phosphorus [51]. Based on the analysis results of XPS and FT-IR spectra, the O atoms were introduced to the surface of the RP NS via P═O and P-O-P bond. As shown in Fig. 6b, the HOMO orbitals and the LUMO orbitals were also respectively distributed on the bulk RP and RP-O NS, providing the further evidence for the direction of electron transfer [52]. And it could be found that LUMO was also orbitals distributed around O atoms. Meantime, this uncovered that the electrons could be enriched in the RP NS under the light irradiation with O atoms (Fig. 6c), while holes were gathered into the bulk phase, illustrating that the surface oxidation

is crucial in photocatalytic process.

Furthermore, to quantify the carrier density of the RP-S-12 h, Mott-Schottky plots was explored in Fig. 6d. The calculated carrier densities for RP-S-12 h ($N_d = 1.33 \times 10^{19}$ cm^{-3}) was 6.15 times and 4.57 times of RP and RP NS, respectively [26]. In the steady-state fluorescence spectrum, RP-S-12 h displayed the lowest fluorescence signal compared with the bulk materials and ultra-thin materials, suggesting that the introduce of RP NS could promote the separation of photogenerated electrons and prolong the electron lifetime (Fig. 6e). The carrier lifetime of RP also exhibited the shorter time ($\tau = 4.59$ ns) than that of RP NS ($\tau = 4.80$) and RP-S-12 h ($\tau = 5.00$ ns) in the time-resolved photoluminescence (TRPL) spectra, illustrating that it was much easier to realize the combination of holes and electrons from the bottom of the conduction band (CB) for the bulk RP (Fig. 6f). These results also confirmed the DFT results and were consistent with a series of photoelectric measurement results.

The contribution of the main reactive oxygen species (ROS) was distinguished via quenching experiment in the photocatalytic system. Fig. 7a performed the degradation effect of RP-S-12 h under the different quenchers. The addition of Cr^{6+} and P-benzoquinone significantly inhibited the degradation effect of MO, demonstrating that superoxide
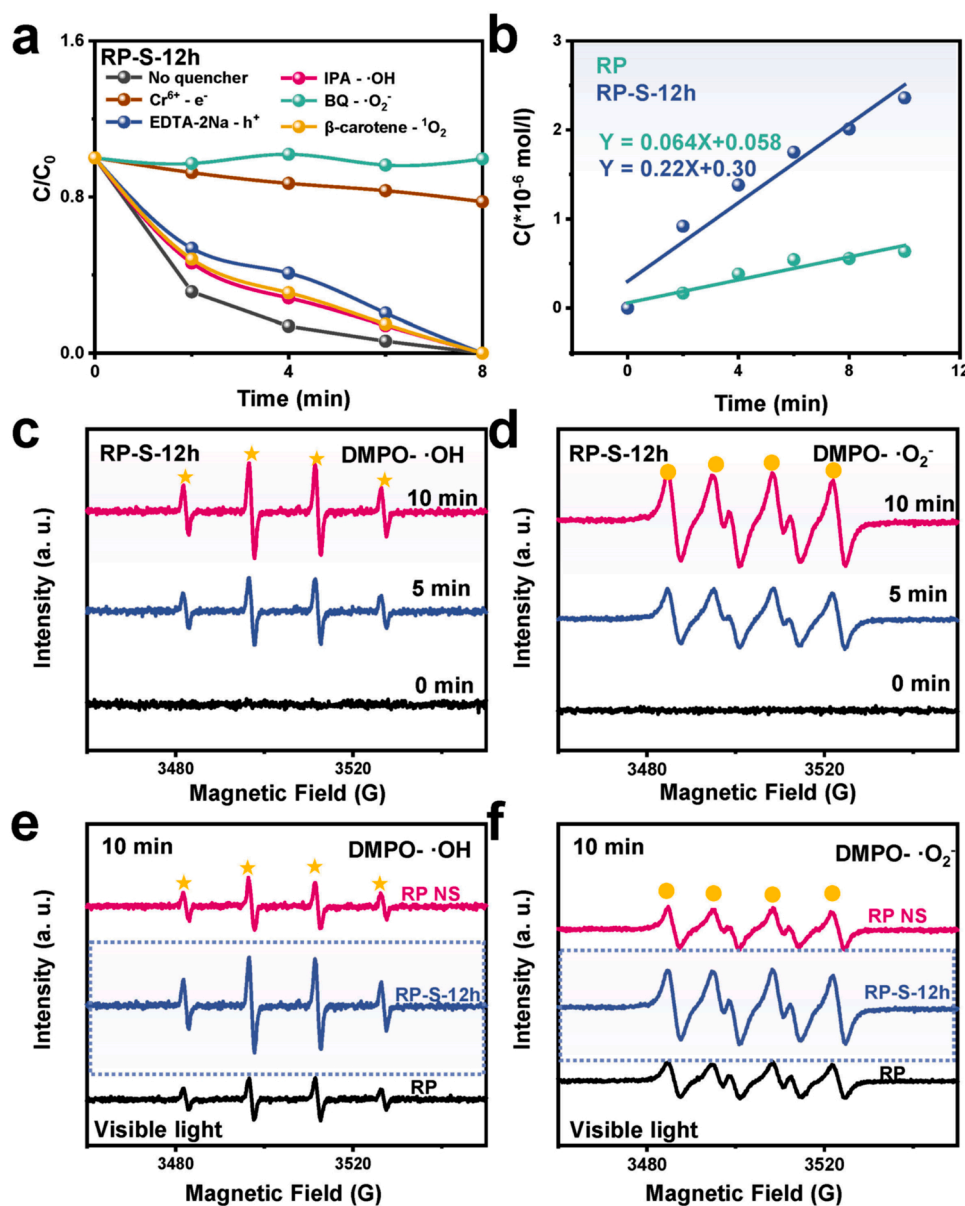
Fig. 7. (a) The quenching experiments to determine the ROS for photocatalytic oxidation of Methyl orange. (b) Analysis of the approximate content for $\bullet O_2^-$ by degrading NBT. EPR spectra of (c) DMPO-$\bullet$OH and (d) DMPO-$\bullet O_2^-$ at diverse time with visible light irradiation. EPR spectra of (e) DMPO-$\bullet$OH and (f) DMPO-$\bullet O_2^-$ over RP, RP-S-12 h and RP NS under 10 min light irradiation.

radical ($\bullet O_2^-$) was the main active species and electronics (e$^-$) played a vital role in the process photocatalytic degradation. The generation rate of $\bullet O_2^-$ was further illustrated by the NBT degradation experiment [27]. RP-S-12 h was 4.26 times (0.052 mmol l^{-1} min^{-1}) that of RP, verifying that the introduce of ultra-thin RP could promote the generation of photoelectrons to trap molecular oxygen to $\bullet O_2^-$ (Fig. 7b). Furthermore, EPR spectroscopic tests with 5, 5-dimethyl-pyrroline-N-oxide (DMPO) as the trapping agent was applied to further prove the generation of $\bullet O_2^-$ and $\bullet$OH for the RP-S-12 h composite. In the dark condition, there was no signal of superoxide radical (The line distinguishing intensity of 1:1:1:1) and hydroxyl radical (The line distinguishing intensity of 1:2:2:1) (Fig. 7c and d) [27]. As expected, the intensity EPR signals was enhanced under visible light compared with RP and RP-S-12 h (Fig. 7e and f), further confirmed the effectiveness of the increased photo-generated charge. Moreover, the concentration of $\bullet O_2^-$ and $\bullet$OH was also further quantified with the extension of light time for RP-S-12 h. The concentration of $\bullet O_2^-$ was 9.69×10^{-6} mol/l at 20 min, which was 1.86 times that at 5 min, suggesting that $\bullet O_2^-$ and $\bullet$OH were

continuously generating during the entire photocatalytic process (Fig. S22).

The mechanism of elevated photocatalytic hydrogen production and degradation activity of pollutants was further explored through UV–visible diffuse reflection and XPS valence band (VB–XPS) spectroscopy. In Fig. 8a, the absorption band edge of RP NS became slightly narrower than bulk RP, supporting that the band gap of RP NS has been mildly widened (RP NS: 1.99 eV; bulk RP: 1.87 eV). The VB over RP NS (1.49 eV) was higher than that of bulk RP (1.23 eV) (Fig. 8b), indicating that the photogenerated electrons generated after being excited could be transferred from the CB of the bulk RP to RP NS, which caused the effective separation of photogenerated electrons and holes, prolonging the life of photogenerated electrons.

Theoretical simulations were also used to further elucidate the functional mechanism of the RP NS for the bulk RP. In the density of states (DOS) of the RP-O NS/bulk RP, Apparently, the existence of O atom (P-O-P and P=O bond) contributed to the original blank energy region formed the interior energy state (Fig. 8c), suggesting that
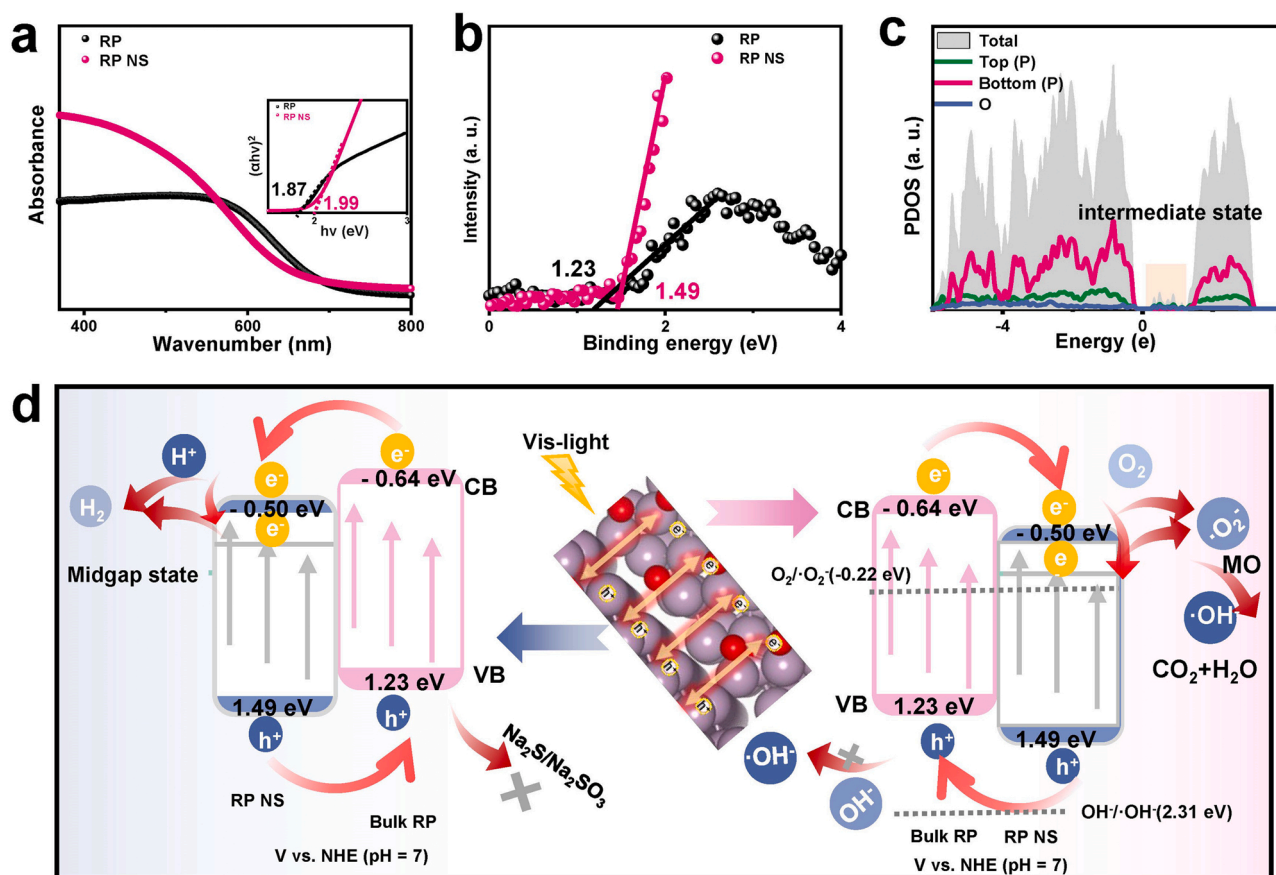
Fig. 8. (a) UV–vis diffuse reflectance spectra and (b) the VB-XPS spectra of the RP and RP NS. (c) The DOS plots of bulk RP/PR-O NS. (d) Schematic diagram of MO degradation and hydrogen production mechanism for RP-S under the visible-light.

photogenerated electrons could be excited to the intermediate state from VB of RP NS and the electrons could be transferred to the intermediate state from the CB of RP NS [53]. In addition, photogenerated electrons of bulk RP could be continuously transferred to the CB position of RP NS.

Based on the above conclusion, the improvement mechanism for photocatalytic hydrogen production and degradation was proposed over the composite in Fig. 8d. The photogenerated electrons will be transferred from the CB position of the bulk RP to the RP NS to form a two-type structure. The remaining electrons will combine with hydrogen ions to generate hydrogens. Correspondingly, it will also combine with oxygen to generate superoxide free radicals and hydroxyl radicals to degrade organic pollutants. Therefore, the recombination of photogenerated electrons and holes has been greatly suppressed. The photocatalytic hydrogen production and degradation energy are accelerated. In addition, the partial oxidation of RP surface provides intermediate state in composites, offering a new channel for the transfer of photogenerated electrons.

4. Conclusion

In summary, the composite of bulk RP and RP NS was established via in-situ hydrothermal method. With the optimal hydrothermal time (12 h), RP-S-12 h showed the excellent hydrogen production rate (0.33 mmol g^{-1} h^{-1}), which was 5.8 times and 2.0 times that of RP and RP NS, respectively. And the hydrogen production rate could still reach 91.4% of the initial hydrogen production rate after three cycles. In addition, RP-S-12 h showed excellent $\bullet O_2^-$ generation ability (0.052 mmol l^{-1} min^{-1}), resulting in higher photocatalytic degradation efficiency. These could be attributed to the appropriate energy band structure and the different surface potentials for the bulk and nanosheet

of RP, effectively accelerating the transfer of photogenerated electrons. The intermediate state caused by the increase of oxygen atoms boosted the separation of carriers. This work combines the same material with different scales to effectively improve the interfacial electron mobility, which is helpful to the design of high-efficiency photocatalysts.

CRediT authorship contribution statement

Fangyuan Chen: Resources, Data curation, Writing – original draft. **Shoutian Sun:** Theoretical calculation, Software, Writing – review & editing. **Kelei Mu:** Methodology, Investigation, Formal analysis. **Yi Li:** Validation, Writing – review & editing, Funding acquisition. **Zhurui Shen:** Conceptualization, Writing-review & editing, Funding acquisition. **Sihui Zhan:** Validation, Conceptualization, Writing – review & editing, Funding acquisition.

Declaration of Competing Interest

The authors declare that they have no known competing financial interests or personal relationships that could have appeared to influence the work reported in this paper.

Acknowledgements

Appendix A. Supporting information

Supplementary data associated with this article can be found in the online version at doi:10.1016/j.apcatb.2022.121373.

References

[1] P. Zhou, H. Chen, Y. Chao, Q. Zhang, W. Zhang, F. Lv, L. Gu, Q. Zhao, N. Wang, J. Wang, Single-atom Pt-I₃ sites on all-inorganic Cs₂SnI₆ perovskite for efficient photocatalytic hydrogen production, Nat. Commun. 12 (2021) 1–8, https://doi.org/10.1038/s41467-021-24702-8.

[2] J. Yan, Y. Ji, M. Batmunkh, P. An, J. Zhang, Y. Fu, B. Jia, Y. Li, S. Liu, J. Ye, Breaking platinum nanoparticles to single-atomic Pt-C₄ co-catalysts for enhanced solar to hydrogen conversion, Angew. Chem. Int. Ed. 60 (2021) 2541–2547, https://doi.org/10.1002/anie.202013206.

[3] Y. Shiraishi, T. Takii, T. Hagi, S. Mori, Y. Kofuji, Y. Kitagawa, S. Tanaka, S. Ichikawa, T. Hirai, Resorcinol-formaldehyde resins as metal-free semiconductor photocatalysts for solar-to-hydrogen peroxide energy conversion, Nat. Mater. 18 (2019) 985–993, https://doi.org/10.1038/s41563-019-0398-0.

[4] Y. Wang, C. Zhu, G. Zuo, Y. Guo, W. Xiao, Y. Dai, J. Kong, X. Xu, Y. Zhou, A. Xie, 0D/2D Co₃O₄/TiO₂ Z-Scheme heterojunction for boosted photocatalytic degradation and mechanism investigation, Appl. Catal. B Environ. 278 (2020), 119298, https://doi.org/10.1016/j.apcatb.2020.119298.

[5] A. Shoneye, J. Sen Chang, M.N. Chong, J. Tang, Recent progress in photocatalytic degradation of chlorinated phenols and reduction of heavy metal ions in water by TiO₂-based catalysts, Int. Mat. Rev. 67 (1) (2021) 47–64, https://doi.org/10.1080/09506608.2021.1891368.

[6] H. Liu, Y. Feng, J. Shao, Y. Chen, Z.L. Wang, H. Li, X. Chen, Z. Bian, Self-cleaning triboelectric nanogenerator based on TiO₂ photocatalysis, Nano Energy 70 (2020), 104499, https://doi.org/10.1016/j.nanoen.2020.104499.

[7] R. Trofimovaite, C.M. Parlett, S. Kumar, L. Frattini, M.A. Isaacs, K. Wilson, L. Olivi, B. Coulson, J. Debgupta, R.E. Douthwaite, Single atom Cu (I) promoted mesoporous titanias for photocatalytic methyl orange depollution and H₂ production, Appl. Catal. B Environ. 232 (2018) 501–511, https://doi.org/10.1016/j.apcatb.2018.03.078.

[8] B. Xu, Y. Li, Y. Gao, S. Liu, D. Lv, S. Zhao, H. Gao, G. Yang, N. Li, L. Ge, Ag-AgI/Bi₃O₄Cl for efficient visible light photocatalytic degradation of methyl orange: the surface plasmon resonance effect of Ag and mechanism insight, Appl. Catal. B Environ. 246 (2019) 140–148, https://doi.org/10.1016/j.apcatb.2019.01.060.

[9] Q. Wang, L. Huang, X. Quan, G.Li Puma, Sequential anaerobic and electro-Fenton processes mediated by W and Mo oxides for degradation/mineralization of azo dye methyl orange in photo assisted microbial fuel cells, Appl. Catal. B Environ. 245 (2019) 672–680, https://doi.org/10.1016/j.apcatb.2019.01.026.

[10] E. Yun, H. Yoo, H. Bae, H. Kim, J. Lee, Exploring the role of persulfate in the activation process: radical precursor versus electron acceptor, Environ. Sci. Technol. 51 (2017) 10090–10099, https://doi.org/10.1021/acs.est.7b02519.

[11] X. Duan, C. Su, J. Miao, Y. Zhong, Z. Shao, S. Wang, H. Sun, Insights into perovskite-catalyzed peroxymonosulfate activation: maneuverable cobalt sites for promoted evolution of sulfate radicals, Appl. Catal. B Environ. 220 (2018) 626–634, https://doi.org/10.1016/j.apcatb.2017.08.088.

[12] Y. Wang, X. Liu, J. Liu, B. Han, X. Hu, F. Yang, Z. Xu, Y. Li, S. Jia, Z. Li, Carbon quantum dot implanted graphite carbon nitride nanotubes: excellent charge separation and enhanced photocatalytic hydrogen evolution, Angew. Chem. Int. Ed. 130 (2018) 5867–5873, https://doi.org/10.1002/anie.201802014.

[13] L. Kong, Y. Ji, Z. Dang, J. Yan, P. Li, Y. Li, S. Liu, g-C₃N₄ loading black phosphorus quantum dot for efficient and stable photocatalytic H₂ generation under visible light, Adv. Fun. Mater. 28 (2018), 1800668, https://doi.org/10.1002/adfm.201800668.

[14] M. Akri, S. Zhao, X. Li, K. Zang, A.F. Lee, M.A. Isaacs, W. Xi, Y. Gangarajula, J. Luo, Y. Ren, Y.T. Cui, L. Li, Y. Su, X. Pan, W. Wen, Y. Pan, K. Wilson, L. Li, B. Qiao, H. Ishii, Y.F. Liao, A. Wang, X. Wang, T. Zhang, Atomically dispersed nickel as coke-resistant active sites for methane dry reforming, Nat. Commun. 10 (1) (2019) 1–10, https://doi.org/10.1038/s41467-019-12843-w.

[15] Y. Xu, M. Kraft, R. Xu, Metal-free carbonaceous electrocatalysts and photocatalysts for water splitting, Chem. Soc. Rev. 45 (2016) 3039–3052, https://doi.org/10.1039/c5cs00729a.

[16] F. Hu, R. Shi, Z. Wang, Y. Weng, C.M. Che, Y. Chen, Direct Z-scheme hetero-phase junction of black/red phosphorus for photocatalytic water splitting, Angew. Chem. Int. Ed. 131 (2019) 11917–11921, https://doi.org/10.1002/anie.201906416.

[17] M. Wang, Z. Qin, Z. Diao, R. Li, J. Zhong, D. Ma, Y. Chen, Red phosphorus/carbon nitride van der Waals heterostructure for photocatalytic pure water splitting under wide-spectrum light irradiation, ACS Sustain. Chem. Eng. 8 (2020) 13459–13466, https://doi.org/10.1021/acssuschemeng.0c04372.

[18] Y. Zhu, J. Li, C. Dong, J. Ren, Y. Huang, D. Zhao, R. Cai, D. Wei, X. Yang, C. Lv, Red phosphorus decorated and doped TiO₂ nanofibers for efficient photocatalytic hydrogen evolution from pure water, Appl. Catal. B Environ. 255 (2019), 117764, https://doi.org/10.1016/j.apcatb.2019.117764.

[19] C. Wu, L. Jing, J. Deng, Y. Liu, S. Li, S. Lv, Y. Sun, Q. Zhang, H. Dai, Elemental red phosphorus-based photocatalysts for environmental remediation: a review, Chemosphere 274 (2021), 129793, https://doi.org/10.1016/j.chemosphere.2021.129793.

[20] Z. Shen, Z. Hu, W. Wang, S. Lee, D. Chan, Y. Li, T. Gu, C.Y. Jimmy, Crystalline phosphorus fibers: controllable synthesis and visible-light-driven photocatalytic activity, Nanoscale 6 (2014) 14163–14167, https://doi.org/10.1039/c4nr04250f.

[21] Z. Hu, L. Yuan, Z. Liu, Z. Shen, J.C. Yu, An elemental phosphorus photocatalyst with a record high hydrogen evolution efficiency, Angew. Chem. Int. Ed. 128 (2016) 9732–9737, https://doi.org/10.1002/ange.201605031.

[22] J. Li, X. Liu, L. Tan, Y. Liang, Z. Cui, X. Yang, S. Zhu, Z. Li, Y. Zheng, K.W.K. Yeung, Photocatalysis: light-activated rapid disinfection by accelerated charge transfer in red phosphorus/ZnO heterointerface, Small, Methods 3 (2019), 1970008, https://doi.org/10.1002/smtd.201970008.

[23] W. Li, Y. Zhang, G. Tian, S. Xie, Q. Xu, L. Wang, J. Tian, Y. Bu, Fabrication of graphene-modified nano-sized red phosphorus for enhanced photocatalytic performance, J. Mol. Catal. A: Chem. 423 (2016) 356–364, https://doi.org/10.1016/j.molcata.2016.07.039.

[24] D. Xia, Z. Shen, G. Huang, W. Wang, J.C. Yu, P.K. Wong, Red phosphorus: an earth-abundant elemental photocatalyst for "green" bacterial inactivation under visible light, Environ. Sci. Technol. 49 (2015) 6264–6273, https://doi.org/10.1021/acs.est.5b00531.

[25] Y. Guo, W. Shi, Y. Zhu, Internal electric field engineering for steering photogenerated charge separation and enhancing photoactivity, EcoMat 1 (2019), e12007, https://doi.org/10.1002/eom2.12007.

[26] N. Zhang, M. Qi, L. Yuan, X. Fu, Z. Tang, J. Gong, Y. Xu, Broadband light harvesting and unidirectional electron flow for efficient electron accumulation for hydrogen generation, Angew. Chem. Int. Ed. 58 (2019) 10003–10007, https://doi.org/10.1002/ange.201905981.

[27] X. Ding, K. Zhao, L. Zhang, Enhanced photocatalytic removal of sodium pentachlorophenate with self-doped Bi₂WO₆ under visible light by generating more superoxide ions, Environ. Sci. Technol. 48 (2014) 5823–5831, https://doi.org/10.1021/es405714q.

[28] G. Kresse, J. Furthmüller, Efficient iterative schemes for ab initio total-energy calculations using a plane-wave basis set, Phys. Rev. B 54 (1996) 11169, https://doi.org/10.1103/PhysRevB.54.11169.

[29] P.E. Blöchl, Projector augmented-wave method, Phys. Rev. B 50 (1994) 17953, https://doi.org/10.1103/PhysRevB.50.17953.

[30] G. Kresse, J. Furthmüller, Efficiency of ab-initio total energy calculations for metals and semiconductors using a plane-wave basis set, Comput. Mater. Sci. 6 (1996) 15–50, https://doi.org/10.1016/0927-0256(96)00008-0.

[31] S. Grimme, J. Antony, S. Ehrlich, H. Krieg, A consistent and accurate ab initio parametrization of density functional dispersion correction (DFT-D) for the 94 elements H-Pu, J. Chem. Phys. 132 (2010), 154104, https://doi.org/10.1063/1.3382344.

[32] E.N. Oelker, E. Soignard, K.A. Mckiernan, C.J. Benmore, J.L. Yarger, Pressure-induced crystallization of amorphous red phosphorus, Solid State Commun. 152 (2012) 390–394, https://doi.org/10.1063/1.3382344.

[33] F. Chen, K. Mu, D. Zhang, X. Mi, Y. Li, Z. Shen, S. Zhan, Ultra-thin red phosphor nanosheets as an efficient photocatalyst for hydrogen evolution under visible light, Top. Catal. 64 (2021) 7–14, https://doi.org/10.1007/s11244-021-01454-9.

[34] X. Zhang, X. Xie, H. Wang, J. Zhang, B. Pan, Y. Xie, Enhanced photoresponsive ultrathin graphitic-phase C₃N₄ nanosheets for bioimaging, J. Am. Chem. Soc. 135 (2013) 18–21, https://doi.org/10.1021/ja308249k.

[35] B. Duan, J. Yang, J.R. Salvador, Y. He, B. Zhao, S. Wang, P. Wei, F.S. Ohuchi, W. Zhang, R.P. Hermann, O. Gourdon, S.X. Mao, Y. Cheng, C. Wang, J. Liu, P. Zhai, X. Tang, Q. Zhang, J. Yang, Electronegative guests in CoSb₃, Energ, Environ. Sci. 9 (2016) 2090–2098, https://doi.org/10.1039/C6EE00322B.

[36] M.T. Edmonds, A. Tadich, A. Carvalho, A. Ziletti, K.M. O'Donnell, S.P. Koenig, D. F. Coker, B. Özyilmaz, A.C. Neto, M. Fuhrer, Creating a stable oxide at the surface of black phosphorus, ACS Appl. Mater. Inter. 7 (2015) 14557–14562, https://doi.org/10.1021/acsami.5b01297.

[37] J.I. Jung, D.D. Edwards, X-ray photoelectron (XPS) and diffuse reflectance infra fourier transformation (DRIFT) study of Ba₀.₅Sr₀.₅CoₓFe₁₋ₓO₃₋δ (BSCF: x=0-0.8) ceramics, J. Solid State Chem. 184 (2011) 2238–2243, https://doi.org/10.1016/j.jssc.2011.06.016.

[38] T. Wu, J. Fan, Q. Li, P. Shi, Q. Xu, Y. Min, Palladium nanoparticles anchored on anatase titanium dioxide-black phosphorus hybrids with heterointerfaces: Highly electroactive and durable catalysts for ethanol electrooxidation, Adv. Energy Mater. 8 (2018), 1701799, https://doi.org/10.1002/aenm.201701799.

[39] Z. Sofer, J. Luxa, D. Bouša, D. Sedmidubský, P. Lazar, T. Hartman, H. Hardtdegen, M. Pumera, The covalent functionalization of layered black phosphorus by nucleophilic reagents, Angew. Chem. Int. Ed. 56 (2017) 9891–9896, https://doi.org/10.1002/ange.201705722.

[40] W. Liu, S. Ju, X. Yu, Phosphorus-amine-based synthesis of nanoscale red phosphorus for application to sodium-ion batteries, ACS Nano 14 (2020) 974–984, https://doi.org/10.1021/acsnano.9b08282.

[41] J. Chai, F. Lu, B. Li, D.Y. Kwok, Wettability interpretation of oxygen plasma modified poly (methyl methacrylate), Langmuir 20 (2004) 10919–10927, https://doi.org/10.1021/la048947s.

[42] Z. Zhu, M. Xiang, P. Li, L. Shan, P. Zhang, Surfactant-modified three-dimensional layered double hydroxide for the removal of methyl orange and rhodamine B: Extended investigations in binary dye systems, J. Solid State Chem. 288 (2020), 121448, https://doi.org/10.1016/j.jssc.2020.121448.

[43] M. Wang, S. Day, Z. Wu, X. Wan, X. Ye, B. Cheng, A new type of porous Zn (II) metal-organic gel designed for effective adsorption to methyl orange dye, Colloids Surf. A 628 (2021), 127335, https://doi.org/10.1016/j.colsurfa.2021.127335.

[44] Y. Sha, I. Mathew, Q. Cui, M. Clay, F. Gao, X.J. Zhang, Z. Gu, Rapid degradation of azo dye methyl orange using hollow cobalt nanoparticles, Chemosphere 144 (2016) 1530–1535, https://doi.org/10.1016/j.chemosphere.2015.10.040.

[45] S. Zhang, X. Zhang, L. Lei, X.F. Yu, J. Chen, C. Ma, F. Wu, Q. Zhao, B. Xing, pH dependent degradation of layered black phosphorus: essential role of hydroxide ions, Angew. Chem. Int. Ed. 58 (2019) 467–471, https://doi.org/10.1002/ange.201809989.

[46] F. Wang, W.K.H. Ng, C.Y. Jimmy, H. Zhu, C. Li, L. Zhang, Z. Liu, Q. Li, Red phosphorus: an elemental photocatalyst for hydrogen formation from water, Appl. Catal. B: Environ. 111 (2012) 409–414, https://doi.org/10.1016/j.apcatb.2011.10.028.

[47] H. Zhou, J. Peng, J. Li, J. You, L. Lai, R. Liu, Z. Ao, G. Yao, B. Lai, Metal-free black-red phosphorus as an efficient heterogeneous reductant to boost Fe^{3+}/Fe^{2+} cycle for peroxymonosulfate activation, Water Res 188 (2021), 116529, https://doi.org/10.1016/j.watres.2020.116529.

[48] P. Wang, Z. Shen, Y. Xia, H. Wang, L. Zheng, W. Xi, S. Zhan, Atomic insights for optimum and excess doping in photocatalysis: a case study of few-layer Cu-$ZnIn_2S_4$, Adv. Fun. Mater. 29 (3) (2019), 1807013, https://doi.org/10.1002/adfm.201807013.

[49] J. Li, G. Zhan, Y. Yu, L. Zhang, Superior visible light hydrogen evolution of Janus bilayer junctions via atomic-level charge flow steering, Nat. Commun. 7 (1) (2016) 1–9, https://doi.org/10.1038/ncomms11480.

[50] W. Jiang, Y. Zhao, X. Zong, H. Nie, L. Niu, L. An, D. Qu, X. Wang, Z. Kang, Z. Sun, Photocatalyst for high-performance H_2 production: Ga-doped polymeric carbon nitride, Angew. Chem. Int. Ed. 60 (2021) 6124–6129, https://doi.org/10.1002/ange.202015779.

[51] P.E.M. Amaral, G.P. Nieman, G.R. Schwenk, H. Jing, R. Zhang, E.B. Cerkez, D. Strongin, H.F. Ji, High electron mobility of amorphous red phosphorus thin films, Angew. Chem. Int. Ed. 58 (2019) 6766–6771, https://doi.org/10.1002/anie.201902534.

[52] Y. Li, X. Xu, J. Wang, W. Luo, L. Wang, Post-redox engineering electron configurations of atomic thick C_3N_4 nanosheets for enhanced photocatalytic hydrogen evolution, Appl. Catal. B Environ. 270 (2020), 118855, https://doi.org/10.1016/j.apcatb.2020.118855.

[53] J. Gong, C. Yang, J. Zhang, W. Pu, Origin of photocatalytic activity of W/N-codoped TiO_2: H_2 production and DFT calculation with GGA+U, Appl. Catal. B Environ. 152–153 (2014) 73–81, https://doi.org/10.1016/j.apcatb.2014.01.028.